energies

MDPI

Article

Analytical Model for Phase Synchronization of a Pair of Vertical-Axis Wind Turbines

Masaru Furukawa [1,*], Yutaka Hara [1] and Yoshifumi Jodai [2]

[1] Faculty of Engineering, Tottori University, 4-101 Koyama-Minami, Tottori 680-8552, Japan; hara@tottori-u.ac.jp
[2] Department of Mechanical Engineering, Kagawa National Institute of Technology (KOSEN), Kagawa College, 355 Chokushi, Takamatsu 761-8058, Japan; jodai@t.kagawa-nct.ac.jp
* Correspondence: furukawa@tottori-u.ac.jp; Tel.: +81-857-31-5731

Abstract: The phase-synchronized rotation of a pair of closely spaced vertical-axis wind turbines has been found in wind tunnel experiments and computational fluid dynamics (CFD) simulations. During phase synchronization, the two wind turbine rotors rotate inversely at the same mean angular velocity. The blades of the two rotors pass through the gap between the turbines almost simultaneously, while the angular velocities oscillate with a small amplitude. A pressure drop in the gap region, explained by Bernoulli's law, has been proposed to generate the interaction torque required for phase synchronization. In this study, an analytical model of the interaction torques was developed. In our simulations using the model, (i) phase synchronization occurred, (ii) the angular velocities of the rotors oscillated during the phase synchronization, and (iii) the oscillation period became shorter and the amplitude became larger as the interaction became stronger. These observations agree qualitatively with the experiments and CFD simulations. Phase synchronization was found to occur even for a pair of rotors with slightly different torque characteristics. Our simulation also shows that the induced flow velocities influence the dependence of the angular velocities during phase synchronization on the rotation directions of the rotors and the distance between the rotors.

Keywords: vertical-axis wind turbine; phase synchronization; analytical model; Bernoulli's law

Citation: Furukawa, M.; Hara, Y.; Jodai, Y. Analytical Model for Phase Synchronization of a Pair of Vertical-Axis Wind Turbines. *Energies* **2022**, *15*, 4130. https://doi.org/10.3390/en15114130

Academic Editor: Davide Astolfi

Received: 2 May 2022
Accepted: 31 May 2022
Published: 4 June 2022

1. Introduction

A pair of closely spaced vertical-axis wind turbines (VAWTs) can yield more power than two isolated VAWTs [1]. This idea was extended to a wind farm where many pairs of small-sized VAWTs were placed in a limited area in order to yield a high power density [2]. VAWTs accept wind from all directions; thus, it is possible to place them in proximity to each other. In order to investigate the performance and characteristics of such closely spaced VAWTs, wind tunnel experiments [3–8] and computational fluid dynamics (CFD) simulations of a pair of VAWTs were performed in two dimensions [9–14], as well as in three dimensions [6,15].

In Ref. [4,5], wind tunnel experiments of a pair of two-bladed H-type Darrieus turbines were reported, and synchronization of the rotations was found in both counter-down (CD) and counter-up (CU) layouts. Note that, in the CD layout, the blades of the two rotors move in the downwind direction in the gap region between the rotors. In the CU layout, the blades move in the upwind direction in the gap region. It was found that the rotational speeds equalize and the power output increases. Let us call this phenomenon phase synchronization. It was also found that the phase difference between the rotors oscillates around a mean value, and converges to it during the phase synchronization period. However, the mechanism of phase synchronization was not discussed in their papers.

Jodai et al. performed wind tunnel experiments on a pair of closely spaced, small-sized rotors made by a 3D printer and found that phase synchronization occurs when the distance between the rotors is sufficiently small in the CD layout [7,8]. It was found that

the rotational speed with phase synchronization was 13% greater than that for a single rotor under the extremely small gap condition; the gap distance was 10% of the rotor diameter. This was the first report on the steep rise of the rotational speed under phase synchronization of a pair of closely spaced VAWTs with the extremely small gap. The oscillation of the phase difference was not reported in their papers.

Hara et al. performed a two-dimensional CFD analysis [13,14] to simulate the experiments by Jodai et al. They adopted a dynamic fluid–body interaction (DFBI) model that enabled the angular velocities of the rotors to change dynamically. The simulation results showed that phase synchronization also occurred in the CFD analysis for both the CD and CU layouts. They also found that the angular velocities of the rotors oscillated around the mean value during phase synchronization. Note that the oscillation of the angular velocities around the mean value means the same as the oscillation of the phase difference. From the observations of the CFD simulation results, it was proposed that phase synchronization and the oscillation of the angular velocities occur because of the interaction torques generated by pressure fluctuations in the gap between the rotors. In fact, they found that the velocity increases and the pressure decreases according to Bernoulli's law when blades of the two rotors come closer together in the gap region.

In this study, we developed an analytical model for the interaction torques that can be included in evolution equations of the angular velocities of rotors considered as solid bodies. Such a model is useful to understand the physics of the observed phenomena. Here, we present the details of the derivation, as well as numerical results showing the phase synchronization and the oscillation of the angular velocities. We also perform a simulation of a pair of rotors with slightly different torque characteristics and show that phase synchronization also occurs if interaction torques exist.

This paper is organized as follows. The details of the model, including the derivation of the interaction torques, are explained in Section 2. Then, Section 3 shows the numerical results based on the model. In particular, in Section 3.2, we report that the phase synchronization and oscillation of the angular velocities occur when using our model. We also report the dependence of the angular velocities in the phase synchronization regime on the gap in Section 3.3. The oscillations of the difference in angular velocities are shown in Section 3.4. The conclusions are given in Section 4. Appendix A shows the verification of our model based on comparison with CFD as well as experimental results, while Appendix B summarizes normalized expressions of our model.

2. Model

Let us consider a pair of VAWTs. The geometry of the layout is shown in Figure 1. The upstream wind flows from the left of the figure. The rotation directions of the rotors are shown by the arrows. Co-rotating, Counter Down, and Counter Up layouts are written as CO, CD, and CU, respectively. In the CD layout, the blades of the rotors move in the downwind direction in the gap region between the rotors. In contrast, in the CU layout, the blades move in the upwind direction.

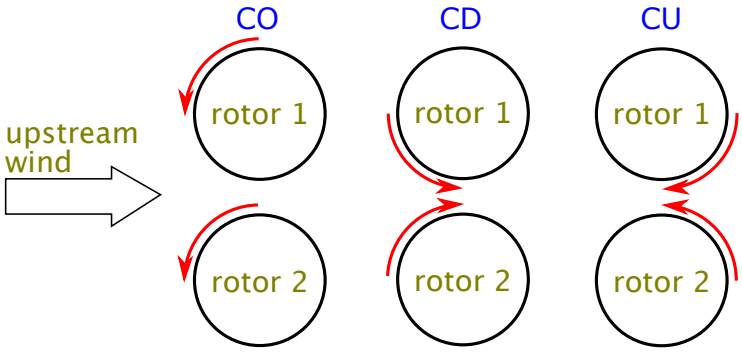

Figure 1. Layouts of rotors.

Figure 2 explains the definitions of variables. The diameter and the radius of a rotor i are denoted by D_i and R_i, respectively. The gap between rotors i and j is given by g_{ij}. In this study, we only considered a pair of rotors. A rotor i has n_i blades, and the position of a blade k is expressed as (x_{ik}, y_{ik}) in the two-dimensional plane, of which the origin is at the center of rotor 1. An azimuthal angle of a blade k of a rotor i is expressed by ψ_{ik}, which is zero in the direction of the y axis and increases in the counterclockwise direction. The blades of a rotor are equally spaced in the azimuthal angle, and thus the angle between the neighboring blades is $2\pi/n_i$. The chord length and the area projected along the rotation direction of a blade k of a rotor i are denoted c_{ik} and S_{ik}, respectively.

The distance between the blade k of the rotor i and the blade ℓ of the rotor j is written as $W_{ik,j\ell}$, which varies in time due to the rotation. As we explain later in this section, we adopted a model to describe a change in the flow velocity according to the temporal change of $W_{ik,j\ell}$, leading to a pressure fluctuation between the blades according to Bernoulli's law. The center of the rotor j is in the direction of an angle ϕ_{ij} seen from the center of rotor i. As with the azimuthal angle ψ_{ik}, the angle ϕ_{ij} is also zero in the direction of the y axis and increases in the counterclockwise direction. The angle of the center of the rotor i seen from the center of the rotor j is ϕ_{ji}, although only ϕ_{12} with $i = 1$ and $j = 2$ is shown in Figure 2.

The wind flows in the direction of the x axis. The upstream speed is denoted by V. The flow velocity experienced by the rotor differs for each rotor. The effective flow velocity immediately in front of rotor i is written as V_i.

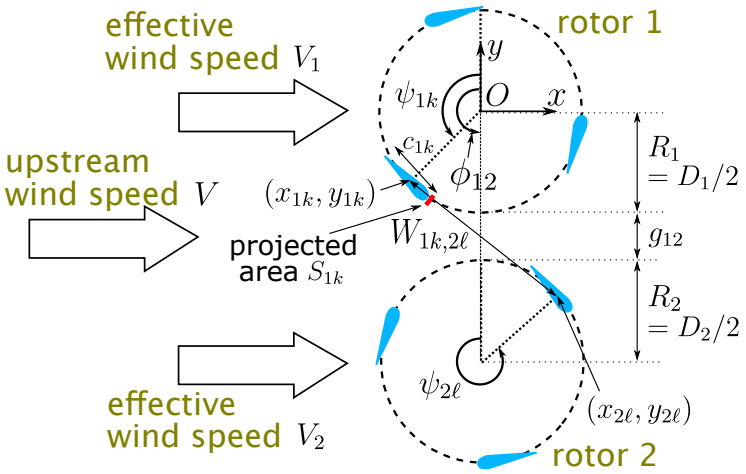

Figure 2. Definitions of variables.

As mentioned above, we only considered a pair of rotors. The evolution equations governing the rotation are

$$I_i \frac{\mathrm{d}\omega_i}{\mathrm{d}t} = Q_i - L_i + Q_{\mathrm{p}i}, \tag{1}$$

$$\frac{\mathrm{d}\psi_i}{\mathrm{d}t} = \omega_i, \tag{2}$$

where $i = 1, 2$ represent the two rotors, ω_i is the angular velocity, $\psi_i := \psi_{i1}$ is the azimuthal angle of a representative blade, I_i is the moment of inertia, Q_i is the rotor torque, L_i is the load torque, and $Q_{\mathrm{p}i}$ is the torque due to the interaction with the other rotor $j\,(\neq i)$ through pressure fluctuation in the gap between them. Note that ψ_i is not necessarily ψ_{i1} but can be another ψ_{ik} with $k \neq 1$; the meaning is the same for any choice of $k = 1, \cdots, n_i$.

In the following section, we explain our torque models. First, we take the rotor torque Q_i as

$$Q_i = -\frac{3\sqrt{3}Q_{\max}(V_i)}{2\omega_0^3(V_i)}\,\omega_i(\omega_i + \omega_0(V_i))(\omega_i - \omega_0(V_i))F_{n_i}(\psi_i). \tag{3}$$

This torque, without the last term $F_{n_i}(\psi_i)$, simulates the torque characteristics in the two-dimensional CFD by Hara et al., as shown in Figure 2 of Ref. [14]. Note that the rotor is operated at an angular velocity, in a sense of average over phase, where the torque in Equation (3) is balanced by a load torque introduced below. Since the balanced state occurs at an angular velocity larger than that at the maximum torque in the present choice of the load torque for a given flow velocity, the rotor torque characteristics at small angular velocity regime is not essential. Here, $F_{n_i}(\psi_i)$ expresses a modulation in the rotor torque depending on the angle of the blades, which we explain shortly. Without this modulation, or setting $F_{n_i}(\psi_i) \equiv 1$, Q_i is a cubic function of ω_i for a given V_i and takes a maximum value $Q_{\max}(V_i)$ when $\omega_i = \omega_0(V_i)/\sqrt{3}$ on the positive ω_i side. When $\omega_i = \omega_0$ at the positive ω_i side, the rotor torque becomes zero. Thus, ω_0 is sometimes called no-load angular velocity.

Here, we take

$$Q_{\max}(V_i) = c_1 V_i^2, \tag{4}$$

$$\omega_0(V_i) = c_2 V_i, \tag{5}$$

where c_1 and c_2 are constants. As shown in Appendix A, we chose these expressions by observing the CFD [13,14], as well as the experimental [7,8] data. The actual values used in our simulation are given in the next section. Note that normalized expressions of Equations (3)–(5), as well as equations to appear below are given in Appendix B, where it is shown that the normalized rotor torque Q_i is expressed by a tip–speed ratio $\lambda_i := R_i\omega_i/V_i$ for the rotor i and normalized $Q_{\max}$ and ω_0 only.

The average of $F_{n_i}(\psi)$ over ψ is taken to be unity. As shown in Appendix A, it is known that the rotor torque by a single blade is finite at the upstream side and becomes maximal when a blade comes to the position $\psi_i = \pi/2$. It decreases to almost zero at the downstream side when the rotor solidity $\sigma_i := n_i c_{ik}/(\pi D_i)$ is large. We assume that

$$F_1(\psi) = \begin{cases} 4\sin^2\psi & (0 \le \psi \le \pi) \\ 0 & (\pi < \psi < 2\pi) \end{cases} \tag{6}$$

for a single blade. Figure 3 shows the azimuthal angle ψ dependence of $F_n(\psi)$. In the figure, $n = 1$ plots Equation (6). The curve of $n = 3$ plots a summation of the modulation function for $n = 1$ over three blades equally spaced in the azimuthal angle and normalized such that $\int_0^{2\pi} F_3(\psi)\mathrm{d}\psi/(2\pi) = 1$. Note that the function for the modulation can be rather flexibly chosen since it is enough to simulate qualitative aspects of the torque modulation. Any function with its maximum at $\psi = \pi/2$ and almost zero in the downstream half may be acceptable.

For the effective wind speed, we use

$$V_i = (1 - a_i)V + \sum_{j \neq i} \frac{\Gamma_j}{2\pi(R_i + R_j + g_{ij})} \cos\phi_{ij}, \tag{7}$$

where a_i is a coefficient of self-induced velocity, and Γ_j is the circulation of rotor j. The second term expresses the velocity induced by another rotor. This assumption, assigning a circulation for a rotor, is similar to the one in Ref. [16]. We take

$$\Gamma_j = c_3 V_j, \tag{8}$$

where c_3 is a constant. This dependence was also obtained by the CFD results as shown in Appendix A. By using the effective wind speed V_i, the rotor torque on rotor i can be calculated. Note that V_i in Equation (7), especially its mutually induced velocity in the second term of the right-hand side, is evaluated by using the coordinate of the center of rotor i. In reality, the effective flow velocity is different for each blade, and the summation of the torques on every blade of a rotor determines the rotor torque. However, in this study, the effective velocity V_i is used for calculating the rotor torque as an average of the effective

velocities for all blades in the rotor, and we assume that V_i is the flow velocity immediately in front of rotor i. Instead of considering the torques on each blade, we take into account the torque modulation of the rotor torque via $F_{n_i}(\psi)$. The modulation expresses the fact that the blade experiences significantly smaller flow than the upstream when it is in the downstream half of the rotation.

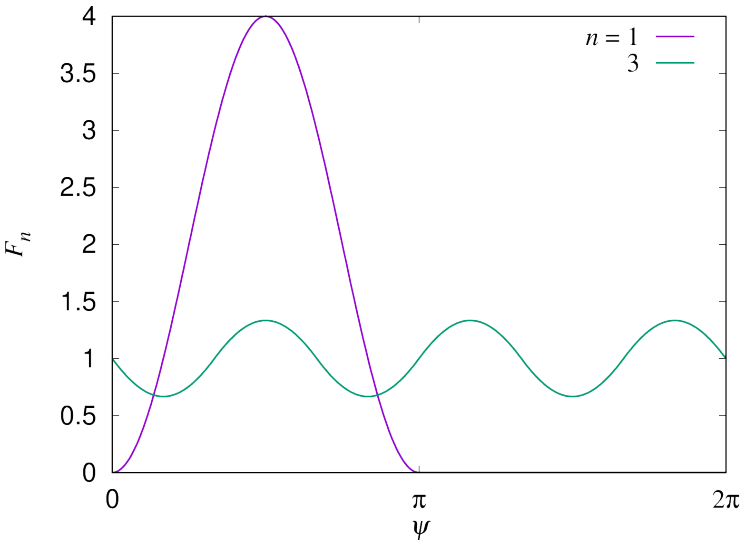

Figure 3. Modulation function $F_n(\psi)$ of the rotor torque on the azimuthal angle of the blade. The curves $n = 1$ and $n = 3$ plot the modulation for a single blade and a summation over three blades, respectively. The average of $F_n(\psi)$ over ψ is taken to be unity.

Secondly, we take the load torque as

$$L_i = c_4 \omega_i^2. \tag{9}$$

The dependence, square of angular velocity, is known as the ideal load torque to obtain highest power at each instance [17]. The CFD simulations by Hara et al. [13,14] also adopted the ideal load torque of the same form. Within our torque model, it is shown that the load torque in Equation (9) works to keep the highest power as follows. According to the rotor torque in Equation (3), the power $Q_i\omega_i$ takes a maximum value when $\omega_i = \omega_0(V_i)/\sqrt{2}$, and the corresponding rotor torque is $Q_i = 3\sqrt{3}Q_{\max}(V_i)/4\sqrt{2}$. By using Equations (4) and (5), these are written such that the maximum power is obtained when $\omega_i = c_2 V_i/\sqrt{2}$ and the corresponding torque is $Q_i = 3\sqrt{3}c_1 V_i^2/4\sqrt{2}$. The ideal operation of the turbine is achieved by balancing the rotor torque Q_i by the load torque L_i for whatever V_i. This is realized by setting $L_i \propto \omega_i^2$, which is obtained by eliminating V_i in Q by using $\omega_i = c_2 V_i/\sqrt{2}$. The coefficient c_4 is determined so that the load torque takes 95% of Q_i when the power becomes maximal for a given V_i in Section 3.1.

Finally, we come to the torque caused by pressure fluctuations between the blades. The positions of the blades of rotors 1 and 2 are given by

$$x_{1k} = -R_1 \sin\psi_{1k}, \tag{10}$$
$$y_{1k} = R_1 \cos\psi_{1k}, \tag{11}$$
$$x_{2\ell} = -R_2 \sin\psi_{2\ell}, \tag{12}$$
$$y_{2\ell} = R_2 \cos\psi_{2\ell} - (R_1 + R_2 + g_{12}). \tag{13}$$

The distance $W_{1k,2\ell}$ between two blades at (x_{1k}, y_{1k}) and $(x_{2\ell}, y_{2\ell})$ is

$$W_{1k,2\ell} = \sqrt{(x_{1k} - x_{2\ell})^2 + (y_{1k} - y_{2\ell})^2}. \tag{14}$$

Here, we consider the flow to be incompressible and assume that

$$V_{\mathrm{av}}(R_1 + R_2 + g_{12}) = (V_{\mathrm{av}} + \delta V)W_{1k,2\ell}, \tag{15}$$

where $V_{\mathrm{av}} := (V_1 + V_2)/2$ is the average flow velocity, and δV expresses the change in the flow velocity between the two blades due to a change in distance between them. Note that the calculation of δV may be improved by taking not only the x component of the flow velocity but also the y component, or taking the distance in the y direction between the blades k and ℓ instead of the distance $W_{1k,2\ell}$ itself. Let us leave this refinement as a future issue. We roughly estimate the change of velocity δV in this study. Then, we obtain the pressure fluctuation δp using Bernoulli's law

$$\frac{1}{2}\rho V_{\mathrm{av}}^2 + p = \frac{1}{2}\rho(V_{\mathrm{av}} + \delta V)^2 + p + \delta p, \tag{16}$$

as

$$\delta p = -\frac{1}{2}\rho\Big(2V_{\mathrm{av}}\delta V + (\delta V)^2\Big). \tag{17}$$

Here, the air pressure is written as p. Note that we neglected the effects of viscous force and unsteadiness of the flow. We adopted the Bernoulli's law to explain interactions between the blades due to pressure fluctuation through the increase in the flow velocity in the x direction observed in the CFD results, as shown in Figure 20 of Ref. [14]. The force on a blade due to this pressure fluctuation is calculated by integrating $-\nabla\delta p$ with the blade volume. The necessary force component is that along the rotation direction $-(\partial\delta p/\partial\psi_{ik})/R_i$ for the blade k of the rotor i. As an example, for $i = 1$, this is calculated as

$$\begin{aligned}\frac{\partial\delta p}{\partial\psi_{1k}} &= -\rho(V_{\mathrm{av}} + \delta V)\frac{\partial\delta V}{\partial\psi_{1k}} \\ &= -\rho\frac{R_1 + R_2 + g_{12}}{W_{1k,2\ell}}V_{\mathrm{av}}\frac{\partial\delta V}{\partial\psi_{1k}}.\end{aligned} \tag{18}$$

By using Equation (15),

$$\begin{aligned}\frac{\partial\delta V}{\partial\psi_{1k}} &= -\frac{R_1 + R_2 + g_{12}}{W_{1k,2\ell}^2}V_{\mathrm{av}}\frac{\partial W_{1k,2\ell}}{\partial\psi_{1k}} \\ &= -\frac{R_1 + R_2 + g_{12}}{W_{1k,2\ell}^3}V_{\mathrm{av}}\left[(x_{1k} - x_{2\ell})\left(\frac{\partial x_{1k}}{\partial\psi_{1k}} - \frac{\partial x_{2\ell}}{\partial\psi_{1k}}\right)\right. \\ &\qquad \left.+(y_{1k} - y_{2\ell})\left(\frac{\partial y_{1k}}{\partial\psi_{1k}} - \frac{\partial y_{2\ell}}{\partial\psi_{1k}}\right)\right].\end{aligned} \tag{19}$$

Then, we can obtain

$$\begin{aligned}\frac{\partial\delta p}{\partial\psi_{1k}} &= \rho V_{\mathrm{av}}^2\frac{(R_1 + R_2 + g_{12})^2}{W_{1k,2\ell}^4}R_1[R_2\sin(\psi_{1k} - \psi_{2\ell}) \\ &\qquad -(R_1 + R_2 + g_{12})\sin\psi_{1k}],\end{aligned} \tag{20}$$

$$\begin{aligned}\frac{\partial\delta p}{\partial\psi_{2\ell}} &= -\rho V_{\mathrm{av}}^2\frac{(R_1 + R_2 + g_{12})^2}{W_{1k,2\ell}^4}R_2[R_1\sin(\psi_{1k} - \psi_{2\ell}) \\ &\qquad -(R_1 + R_2 + g_{12})\sin\psi_{2\ell}].\end{aligned} \tag{21}$$

The torque on a blade due to pressure fluctuations may be approximated by multiplying the blade volume $c_{ik}S_{ik}$ by the rotor radius R_i. Now, we also assume that the total torque on a rotor can be obtained by adding contributions from all blades. Then, we obtain

$$Q_{\mathrm{p1}} = -\alpha \sum_{k=1}^{n_i} \sum_{\ell=1}^{n_j} c_{1k} S_{1k} \rho V_{\mathrm{av}}^2 \frac{(R_1 + R_2 + g_{12})^2}{W_{1k,2\ell}^4} R_1 [R_2 \sin(\psi_{1k} - \psi_{2\ell}) - (R_1 + R_2 + g_{12}) \sin \psi_{1k}], \quad (22)$$

$$Q_{\mathrm{p2}} = \alpha \sum_{\ell=1}^{n_j} \sum_{k=1}^{n_i} c_{2\ell} S_{2\ell} \rho V_{\mathrm{av}}^2 \frac{(R_1 + R_2 + g_{12})^2}{W_{1k,2\ell}^4} R_2 [R_1 \sin(\psi_{1k} - \psi_{2\ell}) - (R_1 + R_2 + g_{12}) \sin \psi_{2\ell}]. \quad (23)$$

Here, a coefficient α is included to control the strength of the interaction between the blades due to the pressure fluctuation, since the summation over all blades may be rather rough. Readers may think that it is strange to add a contribution from a blade at the opposite side of the gap between the rotors; it is natural to count only contributions from blades in the gap region. We also considered a model where rotors are taken as solid cylinders and only considered a narrowed channel between the gap region. This may not be a bad choice for high solidity rotors; however, the flow goes into the region surrounded by the blades of a rotor in reality. Thus, we decided to consider all combinations of blades and to add contributions from all pairs of blades in our model as an average in a sense, although big contributions must arise when two blades come to the gap region, and thus, other contributions may not play major roles. From a numerical computation viewpoint, this assumption, summation over all blades, is far simpler than taking the azimuthal angle of each blade into account to judge whether we should add its contribution or not. The on/off nature of the contributions can yield abrupt changes in torque, leading to a strange time evolution. Thus, we avoid this confusion.

3. Numerical Results

3.1. Characteristics of Rotors

We only consider a pair of rotors and assume that they have completely the same characteristics, except when otherwise stated. The following parameters are chosen. These are the same as those used in the CFD simulations in Hara et al. [13,14]. The number of blades per rotor is $n_1 = n_2 = 3$. The radius of the rotor is $R_1 = R_2 = 25\,\mathrm{mm}$. The chord length is $c_{1k} = c_{2\ell} = 20\,\mathrm{mm}$, and the area projected along the rotation direction is $S_{1k} = S_{2\ell} = 43.4\,\mathrm{mm} \times 3.8\,\mathrm{mm}$ for $k, \ell = 1, 2, 3$. The moment of inertia is $I_1 = I_2 = 5.574 \times 10^{-6}\,\mathrm{kg\,m^2}$. Note that the previous CFD simulation [13,14] was two-dimensional, where the rotor height was 1 m instead of 43.4 mm, as used for the three-dimensional model, and the moment of inertia was set at $I_1 = I_2 = 1.284 \times 10^{-4}\,\mathrm{kg\,m^2} (= 5.574 \times 10^{-6}\,\mathrm{kg\,m^2} \times (1\,\mathrm{m}/43.4\,\mathrm{mm}))$.

From the CFD simulation for a single rotor with the above parameters, under a fixed angular velocity condition, it was found that the maximum power is obtained when $\omega = 366.52\,\mathrm{rad/s}$ for $V = 10\,\mathrm{m/s}$. The time-averaged rotor torque in this case is $Q = 0.525\,\mathrm{mN \cdot m}$. By using these values, we determined $Q_{\max}(V_i)$ and $\omega_0(V_i)$ for the rotor torque, Equation (3), and c_4 for the load torque, Equation (9). We further determined that c_1 and c_2 from $Q_{\max}(V_i)$ and $\omega_0(V_i)$ via Equations (4) and (5).

In the case of our rotor torque (3), the power $Q_i\omega_i$ becomes maximal at $\omega_i = \omega_0(V_i)/\sqrt{2}$ for a given V_i. The rotor torque at this angular velocity is $Q_i = 3\sqrt{3}Q_{\max}(V_i)/4\sqrt{2}$. We chose this to match the CFD value $Q = 0.525\,\mathrm{mN \cdot m}$. Therefore, it is assumed that $\omega_0(10\,\mathrm{m/s}) = \sqrt{2} \times 366.52\,\mathrm{rad/s}$ and $Q_{\max}(10\,\mathrm{m/s}) = (4\sqrt{2}/3\sqrt{3}) \times 0.525\,\mathrm{mN \cdot m}$. From Equation (4), we determine that

$$c_1 = \frac{Q_{\max}(V_i)}{V_i^2} = \frac{4\sqrt{2} \times 0.525\,\mathrm{mN \cdot m}}{3\sqrt{3} \times (10\,\mathrm{m/s})^2} = 5.72 \times 10^{-6}\,\mathrm{kg}. \quad (24)$$

Additionally, from Equation (5), we obtain

$$c_2 = \frac{\sqrt{2} \times 366.52\,\mathrm{rad/s}}{10\,\mathrm{m/s}} = 51.8\,\frac{\mathrm{rad}}{\mathrm{m}}. \quad (25)$$

Furthermore, in the CFD simulation, the angular velocity becomes stationary when the load torque is chosen to be 95% of the optimum rotor torque. We assume the same and thus obtain

$$c_4 = \frac{L_i}{\omega_i^2} = \frac{0.95 \times 0.525\,\mathrm{mN \cdot m}}{(366.52\,\mathrm{rad/s})^2} = 3.71 \times 10^{-9}\,\frac{\mathrm{kg \cdot m^2}}{\mathrm{rad^2}}. \quad (26)$$

We will set the value of c_3 in Section 3.3.

By using these parameters, we obtain the torque curves shown in Figure 4. The rotor torque is plotted for $V = 6, 8, 10$ and $12\,\mathrm{m/s}$ without considering the modulation by $F_{n_i}(\psi)$ and the induced velocities. Note that the rotor torque characteristics at angular velocities lower than the maximum torque for each V are assumed to be different from those of the CFD and the experimental wind turbines to simplify the analysis. The intersection of the rotor torque curve for a given flow velocity and the load torque curve is the a stable steady state. For example, $\omega \simeq 370\,\mathrm{rad/s}$ is the angular velocity at the steady state when $V = 10\,\mathrm{m/s}$. Note that the angular velocity at the steady state for a given flow velocity does not change when the rotor torque Q or $Q_{\max}(V)$ is multiplied by a constant factor, since the load torque L was chosen to also be multiplied by the same factor in the present study.

Note that the adopted angular velocity values $\omega = 366.52\,\mathrm{rad/s}$ (3500 rpm) and the torque $Q = 0.525\,\mathrm{mN \cdot m}$ at the maximum power are slightly different from the values at the steady state $\omega_{\mathrm{SI}} = 366.1\,\mathrm{rad/s}$ (3496 rpm) and $Q_{\mathrm{SI}} = 0.485\,\mathrm{mN \cdot m}$ obtained in the CFD simulation based on the DFBI for a single rotor [14]. "SI" stands for single. We can use these values of ω_{SI} and Q_{SI} instead of those used above to determine $Q_{\max}(V)$, $\omega_0(V)$ and c_4 and then c_1 and c_2 via Equations (4) and (5) by assuming the following three conditions: (i) the rotor torque balances the load torque at $\omega = \omega_{\mathrm{SI}}$, (ii) the balanced torque is $Q = Q_{\mathrm{SI}}$, and (iii) Q_{SI} is 95% of the torque at the maximum power. We can immediately obtain $Q_{\max}(V)$ or c_1 from the second condition and c_4 from the third condition, respectively. We can also obtain $\omega_0(V)$ from the first one, which becomes a cubic equation for $\omega_0(V)$ for a given ω_{SI}. The resulting values are $c_1 = 5.56 \times 10^{-6}\,\mathrm{kg}$, $c_2 = 49.5\,\mathrm{rad/m}$, and $c_4 = 3.62 \times 10^{-9}\,\mathrm{kg \cdot m^2/rad^2}$, of which relative differences from the values obtained in Equations (24)–(26) and used in the simulations presented in Sections 3.2–3.4 are within 5%. Note that $\omega_0(V)$ was calculated from the cubic equation by a perturbation technique based on a trivial approximate solution $\omega_0(V)/\sqrt{2} \simeq \omega_{\mathrm{SI}}$ that gives the maximum power in our model.

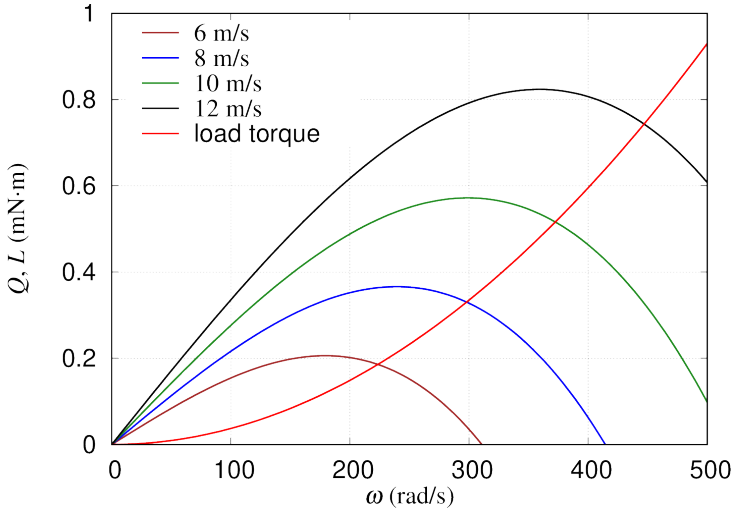

Figure 4. The rotor torques for $V = 6, 8, 10$, and $12\,\mathrm{m/s}$ and load torques are plotted against the angular velocity of the rotor.

3.2. *Phase Synchronization*

In this Section 3.2, we demonstrate that phase synchronization occurs due to the interaction torque generated by the pressure fluctuation. In order to focus on the effect of the interaction torque, we set $a_i = 0$ and $c_3 = 0$, so that $V_i = V$, i.e., the effective flow velocity is the same as the upstream flow velocity. The upstream velocity used in this section is $V = 10\,\mathrm{m/s}$. Furthermore, we set $F_{n_i}(\psi_i) \equiv 1$ to exclude the effects of torque modulation due to the azimuthal angle of the blade.

We solve the evolution Equations (1) and (2) for $i = 1, 2$ by the fourth-order Runge–Kutta method. The step size is $(2\pi/n\omega_{\mathrm{av}}(0))/30$, where $\omega_{\mathrm{av}}(0) = (|\omega_1(0)| + |\omega_2(0)|)/2$.

Figure 5 shows the time evolution of ω_i for $\alpha = 0, 0.05, 0.1$, and 0.2 in the CD layout. The gap between the rotors is $g_{12} = 10\,\mathrm{mm}$. The initial conditions are $\omega_1(0) = 420\,\mathrm{rad/s}$, $\omega_2(0) = -320\,\mathrm{rad/s}$, $\psi_1(0) = \pi$, and $\psi_2(0) = -0.5$. The initial angular velocities have different magnitudes. One of the blades of rotor 1 is at the narrowest position in the gap initially and that of rotor 2 is slightly ahead.

When $\alpha = 0$, the rotors just reach their individual steady states since there is no interaction between the rotors. The rotors have identical characteristics, and thus they rotate at the same angular velocity at the steady state.

When α is finite, the angular velocities oscillate. This simulates the phase synchronization observed in the experiments as well as in the CFD simulations. Such phase synchronization and oscillation of phase difference in the wind tunnel experiments of a pair of two-bladed H-type Darrieus turbines were reported in Section 6.2 of Ref. [4] and in Section 4.4 of Ref. [5]. The phase synchronization and the oscillation of angular velocities in the two-dimensional CFD were reported in Section 3.5 and Figures 17–19 of Ref. [14]. The oscillation period becomes shorter as α increases since the interaction between the rotors becomes stronger. The oscillation period of the angular velocities is about 0.5 s for $\alpha = 0.05$ at $t \simeq 4\,\mathrm{s}$, while it is about 0.25 s for $\alpha = 0.2$. Moreover, the oscillation period becomes shorter over time.

The oscillation amplitude of the angular velocity becomes larger as α is increased. This is also because the interaction becomes stronger as α is increased.

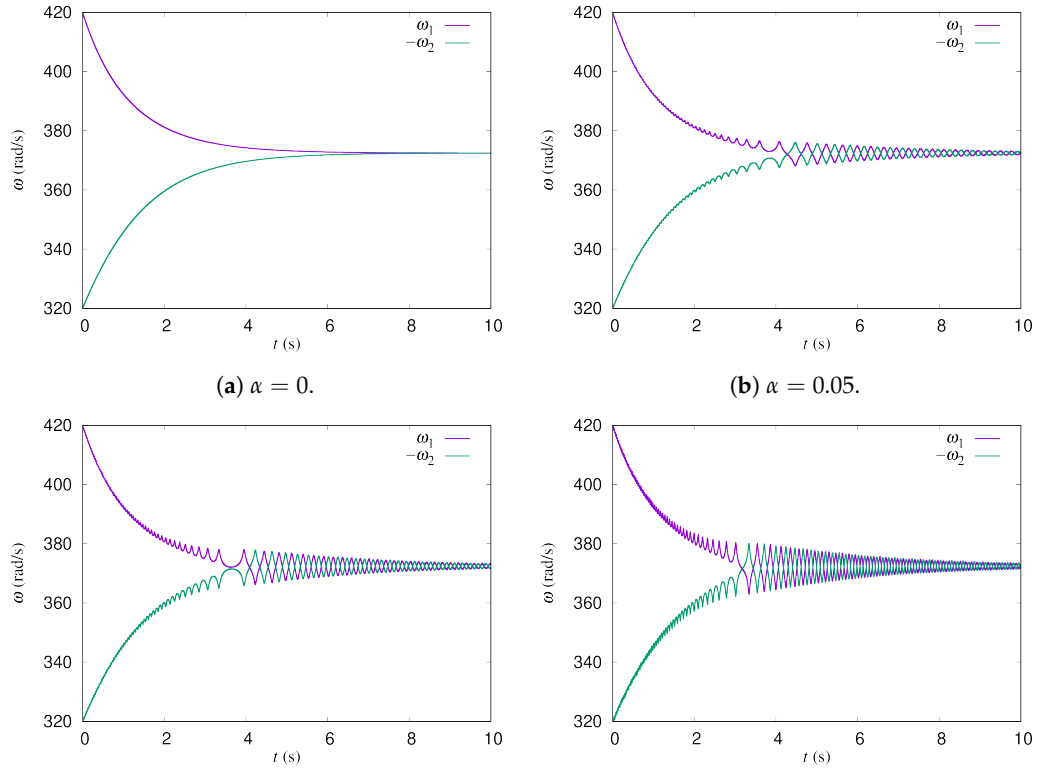

(**a**) $\alpha = 0$. (**b**) $\alpha = 0.05$.

(**c**) $\alpha = 0.1$. (**d**) $\alpha = 0.2$.

Figure 5. Time evolution of ω_i for $\alpha = 0, 0.05, 0.1$, and 0.2 in the CD layout with a 10 mm gap.

Figure 6 shows the time evolution of the phase differences $\delta\psi_k = (\psi_{11} + \psi_{2k}) \bmod 2\pi$ when $\alpha = 0.05$ and $\alpha = 0.2$. The index k takes a value of 1, 2, or 3. Before the phase synchronization, $\delta\psi_k$ runs over the whole range of azimuthal angles. During phase synchronization, on the other hand, $\delta\psi_k$ oscillates around a fixed angle. One of the three blades of rotor 2 has a phase difference of π with blade 1 of rotor 1, which means that those blades meet in the gap region every rotation. We see that the oscillation period of the angular velocity during phase synchronization is shorter for larger α values, as shown in Figure 6. Moreover, the phase synchronization starts earlier for larger α values.

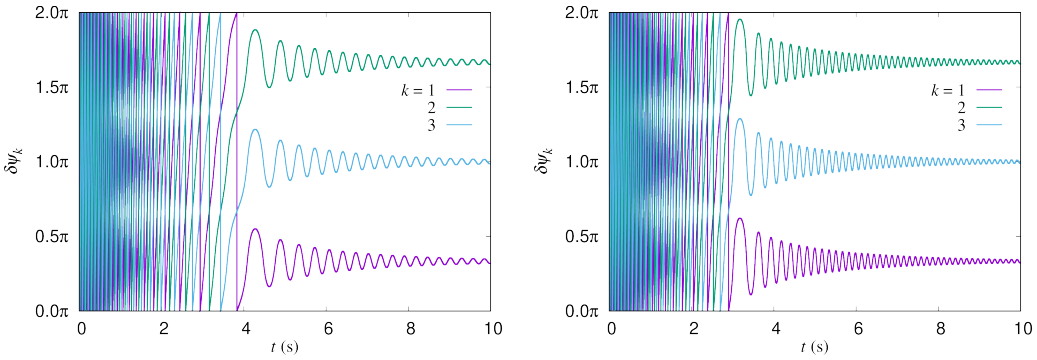

(**a**) $\alpha = 0.05$. (**b**) $\alpha = 0.2$.

Figure 6. Time evolution of phase differences $\delta\psi_k = (\psi_{11} + \psi_{2k}) \bmod 2\pi$ for $\alpha = 0.05$ and 0.2 in the CD layout with 10 mm gap.

Phase synchronization occurs also in the CU layout. Since the induced velocity is not taken into account in the simulations presented in this section, the oscillation period and amplitude are the same as those in the CD layout.

Surprisingly, phase synchronization also occurs in the CO layout. The time evolution of ω for $\alpha = 0.05$ and 0.2 is shown in Figure 7. Compared with the data presented in

Figure 5 for the CD layout, the oscillation period of the angular velocities of the CO layout is longer than those of the CD layout with the same α values. We can also see that the oscillation amplitude of the angular velocities is smaller in the CO layout than that in the CD layout. This is of course because the interaction in the CO layout is much weaker than in the CD and CU layouts. In this simulation, the characteristics of the rotors are identical, and thus, the angular velocity is the same at the steady state without the interaction. In the beginning, the magnitudes of ω_1 and ω_2 are largely different. Thus, they have almost no interaction. However, as the magnitudes of ω_1 and ω_2 become closer to their steady-state values, the time period that the blades of the rotors stay in the narrow gap region together becomes longer, although it must still be much shorter than that for the CD and CU layouts. This makes the interaction effect visible, even in the CO layout.

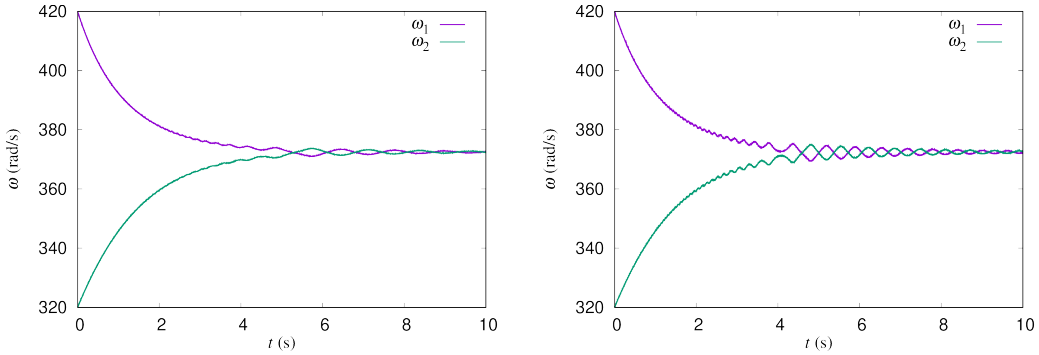

(**a**) $\alpha = 0.05$. (**b**) $\alpha = 0.2$.

Figure 7. Time evolution of ω_i for $\alpha = 0.05$ and 0.2 in the CO layout with 10 mm gap. Induced velocities are not taken into account.

In fact, it becomes difficult for phase synchronization to occur if the angular velocities of the rotors at steady state without interaction are different from each other. We set the rotor torque of rotor 2 as 95% of that of rotor 1 while keeping the load torque unchanged. The other parameters are the same as those used in Figure 7. This makes the angular velocity of rotor 2 about 366 rad/s at its steady state without interaction, which is about 1.7% smaller than that of rotor 1. The time evolution of ω for $\alpha = 0.1$ is plotted in Figure 8a. Phase synchronization does not occur in this case. The angular velocities oscillate around each steady-state value. Note that phase synchronization occurs when $\alpha \geq 0.5$, even in this case.

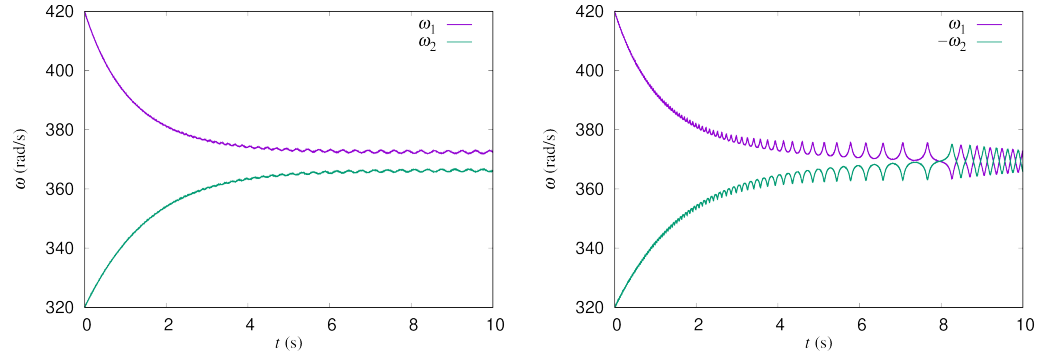

(**a**) CO layout. (**b**) CD layout.

Figure 8. Time evolution of ω_i for the (**a**) CO and (**b**) CD layouts with $\alpha = 0.1$ and $g_{12} = 10$ mm when the rotor torque of rotor 2 is 95% that of rotor 1. The induced velocities are not taken into account.

On the other hand, phase synchronization occurs for the CD layout, even at $\alpha = 0.1$, which is shown in Figure 8b. The angular velocity of the rotors during phase synchronization is about 369 rad/s, which is about an average of the natural values of the two rotors without interaction. Phase synchronization occurs for smaller interactions because the

relative speed of the blades of the two rotors is smaller for the CD layout than for the CO layout, leading to a longer interaction duration.

It may be worth pointing out that α can be used to qualitatively reproduce the parameter dependence of the experimental and CFD results on aspects such as the solidity and upstream flow velocity by assuming that α is dependent on these parameters. This is left as a future issue.

3.3. Dependence of the Synchronized Angular Velocity on the Gap

In this Section 3.3, we focus on the dependence of the synchronized angular velocity on the gap, especially when we take into account the mutually induced velocities generated by each component. Therefore, we set $|c_3| = 0.0427\,\mathrm{m}$ according to the CFD simulation results [13,14]. The sign of c_3 is positive when $\omega > 0$ and negative when $\omega < 0$. On the contrary, we set $a_i = 0$, since the self-induced velocity by the rotor itself should be the same for identical rotors. When $a_1 = a_2$, the effect is only a change in the upstream velocity by a factor of $a_1 = a_2$ for both rotors. Note that the torque modulation $F_{n_i}(\psi_i)$ in Equation (3) with $n_i = 3$ is taken into account in the results presented in this section.

The angular velocity at steady state is plotted against the gap width in Figure 9. Each angular velocity is obtained using the Fourier transform of the time series data at the steady state. We show the results for $\alpha = 0.05$, although they are the same for different α values. Additionally, $F_{n_i}(\psi_i)$ just introduces modulation of the angular velocity, of which the period is one-third of the rotation period of the rotor and does not affect the phase-synchronized angular velocity.

The magnitudes of the angular velocities ω_1 and ω_2 agree well in both the CD and CU layouts. The dashed line at $\omega \simeq 372\,\mathrm{rad/s}$ is the angular velocity without the mutually induced velocity. The angular velocities at each g_{12}/D are larger (smaller) than this value in the CD (CU) layout. This is due to the induced velocity. The effective velocity is larger (smaller) than the upstream velocity in the CD (CU) layout, as found in the CFD simulation [13,14]. Furthermore, the angular velocity increases (decreases) as the gap is narrowed in the CD (CU) layout because the magnitude of the induced velocity becomes larger for smaller gaps. This dependence can be clearly observed for the CD layout in the experiments [7,8] and the CFD simulations, except for the small gap distances [13,14]. For the CU layout, on the other hand, further analysis is required for comparison with the experiments and the CFD simulations.

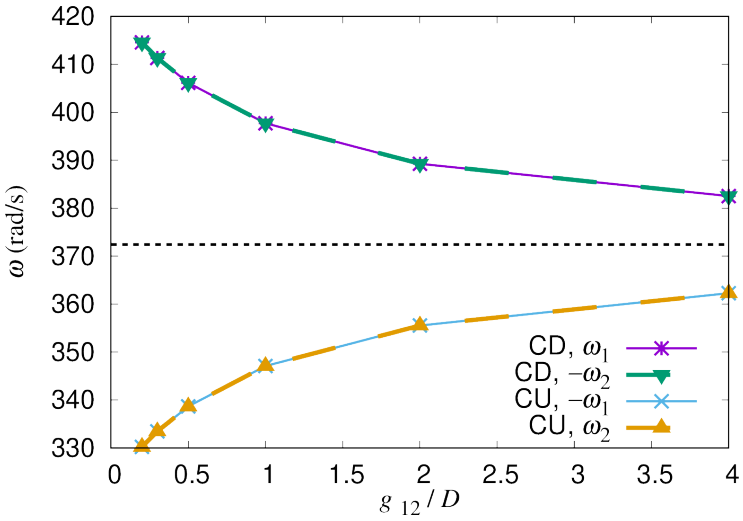

Figure 9. The angular velocity in the phase-synchronized steady state is plotted against the gap g_{12}/D. The dashed line around $\omega \simeq 372\,\mathrm{rad/s}$ shows the angular velocity at the steady state without the mutually induced velocity.

3.4. Oscillation Period of the Difference in Angular Velocities

In this Section 3.4, we analyze the oscillation period of the difference of angular velocities $\Delta\omega := |\omega_1| - |\omega_2|$. The parameters used are the same as those in Section 3.3. Figure 10 shows the time evolution of $\Delta\omega$ for the CD and CU layouts with $g_{12}/D = 0.2$ and 0.3. The parameter $\alpha = 0.05$ was chosen to control the interaction strength for which the oscillation period of $\Delta\omega$ has a comparable order of magnitude with the experiments [4,5] and the CFD simulations [13,14]. The difference $\Delta\omega$ oscillates around 0 during phase synchronization and decays gradually. The oscillation period becomes shorter as time proceeds in all cases, as shown in Figure 10.

First, we found that the oscillation period is longer for the CU layout than the CD layout if the gap distance is the same. For example, the oscillation period is about 0.36 s for the CD layout with $g_{12}/D = 0.2$ at around $t = 5$ s, while it is about 0.55 s for the CU layout.

Second, we found that the oscillation period is longer for a larger gap distance for a given layout. For example, the oscillation period is about 0.36 s when $g_{12}/D = 0.2$ for the CD layout at around $t = 5$ s, while it is about 0.62 s when $g_{12}/D = 0.3$.

The oscillation period of $\Delta\omega$ seems to be related to the mean angular velocity during phase synchronization; $\Delta\omega$ is longer for smaller mean angular velocities. The mean angular velocity is smaller in the CU layout than in the CD layout because of the mutual induced velocity (see Figure 9). Additionaly, the interaction becomes weaker if the gap distance is larger, thereby the oscillation period becomes longer.

Note that it is difficult to find such trends for the amplitude of $\Delta\omega$, since it decays over time. However, we found that the decay is slower for the CU layout than the CD layout if the gap distance is the same. The damping rate seems to be smaller for longer oscillation periods. The oscillation amplitude for the CD layout with $g_{12}/D = 0.2$ is about 7 rad/s at around $t = 5$ s. The relative magnitude for the mean angular velocity $\omega \simeq 415$ rad/s is about 1.7%. The relative magnitude is a bit larger for the CU layout, since the mean angular velocity is smaller while the oscillation amplitude is comparable if the gap distance is the same.

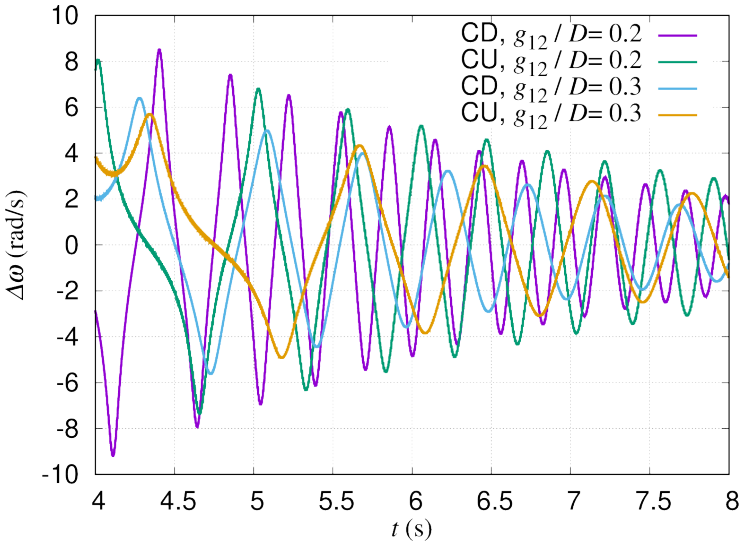

Figure 10. Time evolution of difference of angular velocities $\Delta\omega := |\omega_1| - |\omega_2|$ is shown. The oscillation period is longer for larger gap distances, as well as for the CU layout compared with the CD layout.

4. Conclusions

We developed an analytical model of the interaction torque between two vertical-axis wind turbines through pressure fluctuation. In this model, the pressure fluctuation is obtained according to Bernoulli's law, taking into account the temporal change in distance between the blades. Although rather crude assumptions were made in the development of

the model, our simulations successfully demonstrated the phase synchronization as well as the oscillation of angular velocities around the mean value observed in the experiments and CFD simulations.

Our simulation results show that the angular velocities of the rotors oscillate in time during phase synchronization. When an artificial parameter is changed to strengthen the interaction, the oscillation period becomes shorter and the amplitude becomes larger. This is reasonable physically.

It was also found that phase synchronization occurs even for a pair of rotors with slightly different torque characteristics. This is important because the characteristics of the rotors cannot be identical in experiments.

Our model includes the induced velocities, which change the effective wind speed at each rotor. The simulation results also show that the mutually induced velocity can explain the qualitative dependence of the phase-synchronized angular velocities on the rotational direction of the rotors and the gap distance between them.

The oscillation period of the difference in angular velocities was found to be longer in the CU layout than in the CD layout. Additionally, the oscillation period was found to be longer for larger gap distances. This dependence seems to be related to the mean angular velocity of the rotors during phase synchronization. The mutually induced velocity changed the mean angular velocity in our simulations. The weaker interaction for larger gap distance made the oscillation period longer.

Author Contributions: Conceptualization, M.F., Y.H. and Y.J.; methodology, M.F.; software, M.F.; validation, Y.H. and Y.J.; formal analysis, M.F.; investigation, M.F.; resources, M.F.; data curation, M.F.; writing—original draft preparation, M.F.; writing—review and editing, Y.H. and Y.J.; visualization, M.F.; supervision, Y.H.; project administration, Y.H. and Y.J.; funding acquisition, Y.H. and Y.J. All authors have read and agreed to the published version of the manuscript.

Funding: This work was supported by JSPS KAKENHI Grant Number JP18K05013. The second author was supported in part by the International Platform for Dryland Research and Education (IPDRE), Tottori University.

Institutional Review Board Statement: Not applicable

Informed Consent Statement: Not applicable

Data Availability Statement: The data presented in this study are available from the corresponding author upon reasonable request.

Conflicts of Interest: The authors declare no conflict of interest.

Nomenclature

D_i	Diameter of rotor i
R_i	Radius of rotor i
g_{ij}	Gap between rotors i and j
n_i	Number of blades on rotor i
x	Coordinate in streamwise direction
y	Coordinate in spanwise direction
x_{ik}	x coordinate of blade k of rotor i
y_{ik}	y coordinate of blade k of rotor i
ψ_{ik}	Azimuthal angle of blade k of rotor i
c_{ik}	Chord length of blade k of rotor i
S_{ik}	Projected area of blade k of rotor i along rotation direction
$W_{ik,j\ell}$	Distance between blade k of rotor i and blade ℓ of rotor j
ϕ_{ij}	Angle of rotor j observed from rotor i
V	Upstream flow speed
V_i	Effective flow velocity at rotor i
I_i	Moment of inertia of rotor i
ω_i	Angular velocity of rotor i
Q_i	Rotor torque on rotor i

L_i	Load torque on rotor i
$Q_{\mathrm{p}i}$	Torque due to pressure fluctuation on rotor i
ψ_i	Azimuthal angle of representative blade of rotor i
$Q_{\max}(V_i)$	Maximum rotor torque for given V_i
$\omega_0(V_i)$	No-load angular velocity for given V_i
$F_n(\psi)$	Torque-modulation function for n-blades rotor
c_1	Parameter for $Q_{\max}(V_i)$
c_2	Parameter for $\omega_0(V_i)$
λ_i	Tip-speed ratio of rotor i
ψ	Azimuthal angle fixed in space
σ_i	Solidity of rotor i
$F_1(\psi)$	Torque-modulation function for single-blade rotor
a_i	Parameter for self-induced velocity
Γ_j	Circulation of rotor j
c_3	Parameter for Γ_j
c_4	Parameter for L_i
V_{av}	Average flow velocity $(V_1 + V_2)/2$
δV	Change in flow velocity
δp	Pressure fluctuation
p	Air pressure
α	Parameter controlling strength of interaction between rotors
ω_{SI}	Steady-state angular velocity of single rotor by CFD using DFBI model
Q_{SI}	Steady-state rotor torque of single rotor by CFD using DFBI model
$\omega_{\mathrm{av}}(0)$	Average of initial angular velocities $(\lvert\omega_1(0)\rvert + \lvert\omega_2(0)\rvert)/2$
$\delta\psi_k$	Phase differences between representative blade of rotor 1 and blade k of rotor 2
$\Delta\omega$	Difference of angular velocities $\lvert\omega_1\rvert - \lvert\omega_2\rvert$
C_{qi}	Torque coefficient of rotor i
$\hat{Q}_{\max}$	Normalized maximum rotor torque
λ_0	No-load tip-speed ratio
ρ	Mass density of air
A_i	Swept area of rotor i
$\hat{\Gamma}_j$	Normalized circulation of rotor j
C_{Li}	Normalized load torque for rotor i
c_L	Parameter for C_{Li}

Appendix A. Verification of Parameter Dependence

In this Appendix A, CFD and experimental data to determine dependence of $Q_{\max}$ on flow velocity V in Equation (4), dependence of ω_0 on V in Equation (5), CFD data to determine expression of the torque-modulation function in Equation (6), and dependence of Γ on V in Equation (8) are shown.

First, let us show the dependence of $Q_{\max}$ on flow velocity V read from Figure 2 of Ref. [14] and Figure 3 of Ref. [8]. Figure A1 shows the CFD and experimental data, as well as their fitting curves taken to be quadratic in V. The fitting curves agree well with the CFD and experimental data.

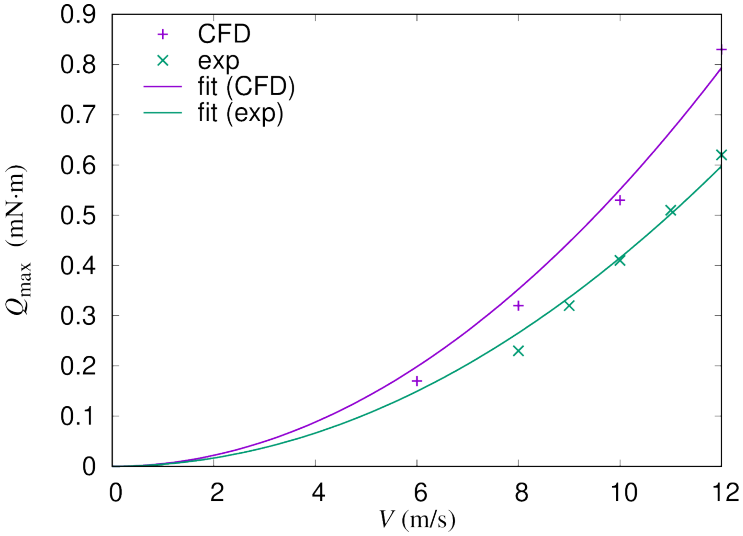

Figure A1. $Q_{\max}$ from Figure 2 of Ref. [14], Figure 3 of Ref. [8], and their fitting curves are shown.

Second, let us show the dependence of ω_0 on flow velocity V, also read from Figure 2 of Ref. [14] and Figure 3 of Ref. [8]. Figure A2 shows the CFD and experimental data, as well as their fitting curves taken to be linear in V. Although the number of data points is not enough, the fitting curves appear to agree well with the CFD and experimental data.

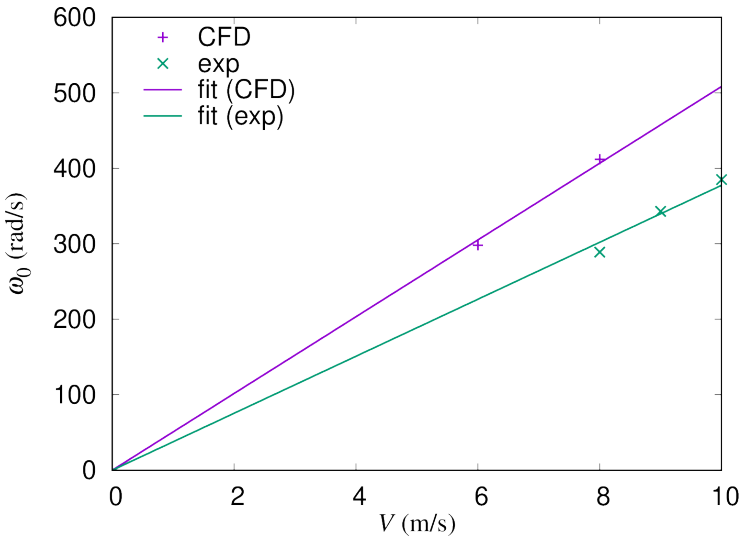

Figure A2. ω_0 from Figure 2 of Ref. [14], Figure 3 of Ref. [8], and their fitting curves are shown.

Third, the torque dependence on the azimuthal angle obtained by the CFD is shown. A rotor with three blades, of which dimensions are the same as described in Section 3.1, was placed in the flow field of which upstream flow velocity was 10 m/s. The modulation of the torque, expressed by Equation (6), tries to simulate this dependence. Figure A3 shows the averaged torques over the 16th–20th rotations of the CFD data, which was not published previously. For $n = 3$, the torque is the summation of torques on all blades of the rotor. The torque for a single blade has its maximum at $\psi \simeq \pi/2$. In the downstream half, the torque on a single blade becomes negative in the CFD, although it is set to be zero in Equation (6) for simplicity.

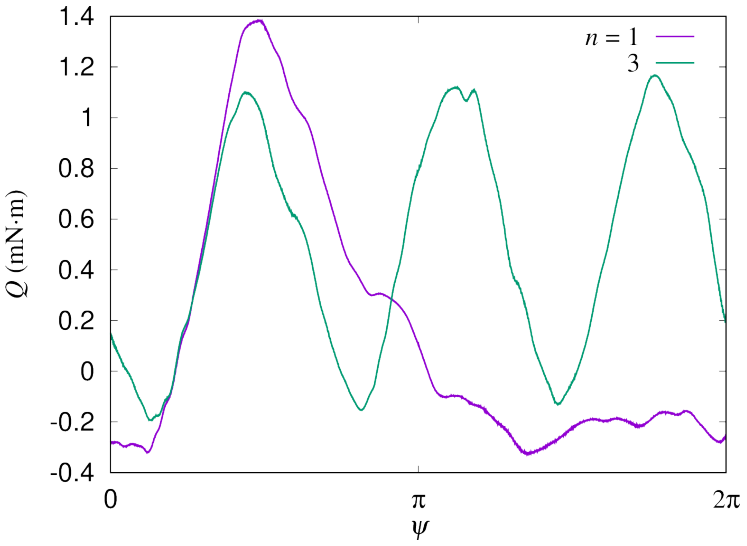

Figure A3. Torque dependence on the azimuthal angle obtained by CFD. Equation (6) tries to simulate this dependence.

Finally, let us show the dependence of Γ on flow velocity. Figure A4 shows Γ obtained by CFD simulations, and their fitting curves taken to be linear in flow velocity. The CFD data were obtained by the time average of the simulation results. In the figure, "inf" means a plot of asymptotic values of Γ at infinity against upstream flow speeds, and the "ep", or evaluation point, means a plot of Γ evaluated on a circle with a 36.1 mm radius centered at the rotor against flow speeds on the upstream side at 36.1 mm from the rotor center. Precisely, the flow speeds of the "ep" case are obtained by averaging over a 50 mm range in the spanwise direction. Note that the horizontal axis is not the upstream velocity for the "ep" case, although it is labeled by V. The fitting curves agree well with the CFD data.

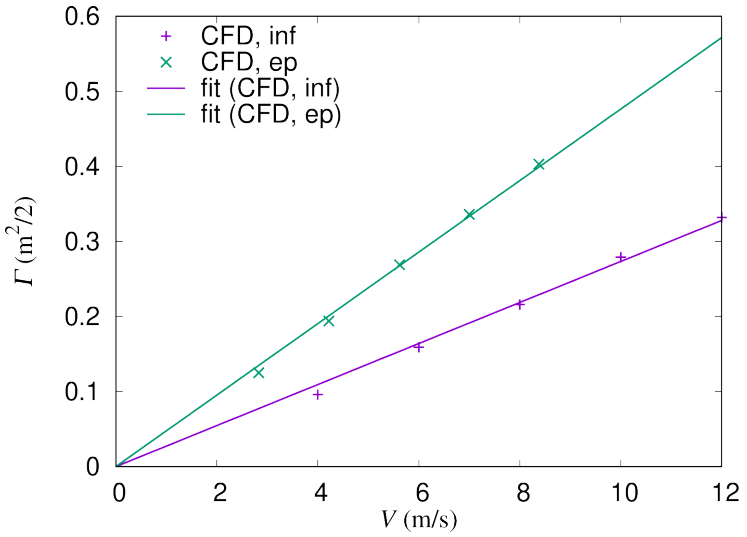

Figure A4. Γ obtained by CFD results and the fitting curves are shown.

Appendix B. Normalized Expression

In this Appendix B, normalized expressions of our model are summarized. First, let us normalize $Q_{\max}(V_i)$ and $\omega_0(V_i)$ given in Equations (4) and (5), respectively, as follows:

$$\begin{aligned} \hat{Q}_{\max} &:= \frac{Q_{\max}(V_i)}{\rho V_i^2 A_i R_i/2} \\ &= \frac{2c_1}{\rho A_i R_i}, \end{aligned} \tag{A1}$$

$$\begin{aligned} \lambda_0 &:= \frac{\omega_0(V_i)}{V_i/R_i} \\ &= c_2 R_i, \end{aligned} \tag{A2}$$

where ρ is the mass density of air, and A_i is the swept area of rotor i. Note that $\hat{Q}_{\max}$ and λ_0 are independent of V_i. By using Equations (A1) and (A2), the torque coefficient C_{qi}, or normalized rotor torque Q_i given in Equation (3) with $F_{n_i}(\psi_i) \equiv 1$, can be expressed as

$$\begin{aligned} C_{qi} &:= \frac{Q_i}{\rho V_i^2 A_i R_i/2} \\ &= -\frac{3\sqrt{3}\hat{Q}_{\max}}{2\lambda_0^3}\lambda_i(\lambda_i+\lambda_0)(\lambda_i-\lambda_0), \end{aligned} \tag{A3}$$

where $\lambda_i := R_i\omega_i/V_i$ is the tip–speed ratio of rotor i. The torque coefficient C_{qi} is expressed only by λ_i, and the dimensionless parameters $\hat{Q}_{\max}$ and λ_0 only. The rotor torque becomes zero when λ becomes equal to the no-load tip–speed ratio λ_0.

Next, the circulation in Equation (8) is normalized as

$$\begin{aligned} \hat{\Gamma}_j &:= \frac{\Gamma_j}{R_i V_i} \\ &= \frac{c_3}{R_j}. \end{aligned} \tag{A4}$$

Note that $\hat{\Gamma}_j$ is independent of V_i.

Lastly, let us normalize the load torque given in Equation (9) as

$$\begin{aligned} C_{Li} &:= \frac{L_i}{\rho V_i^2 A_i R_i/2} \\ &= c_L \lambda_i^2, \end{aligned} \tag{A5}$$

where

$$c_L := \frac{2c_4}{\rho A_i R_i^3}. \tag{A6}$$

Again, the parameter c_L is independent of V_i.

By using these expressions, numerical values of $\hat{Q}_{\max}$, λ_0, $\hat{\Gamma}$, and c_L corresponding to the parameters used in Section 3 are obtained as follows:

$$\hat{Q}_{\max} = 0.176, \tag{A7}$$

$$\lambda_0 = 1.30, \tag{A8}$$

$$\hat{\Gamma} = 1.71, \tag{A9}$$

$$c_L = 0.182. \tag{A10}$$

Note that the mass density of air is assumed to be $\rho = 1.20\,\mathrm{kg/m^3}$. The rotor radius is $R = 50\,\mathrm{mm}$ and the swept area is $A = 50\,\mathrm{mm} \times 43.4\,\mathrm{mm} = 2.17 \times 10^{-3}\,\mathrm{m^2}$.

Let us point out that the simulation results shown in Section 3 can be interpreted, if ω_i is expressed by the tip–speed ratio λ_i, as results with a different set of a flow velocity V_i, a rotor radius R_i, and a swept are A_i that give the same dimensionless parameters $\hat{Q}_{\max}$, λ_0, $\hat{\Gamma}$, and c_L.

References

1. Thomas, R.N. Coupled Vortex Vertical Axis Wind Turbine. US Patent US 6,784,566 B2, 31 August 2004.
2. Dabiri, J.O.; Greer, J.R.; Koseff, J.R.; Moin, P.; Peng, J. A new approach to wind energy: Opportunities and challenges. *AIP Conf. Proc.* **2015**, *1652*, 51–57. [CrossRef]
3. Ahmadi-Baloutaki, M.; Carriveau, R.; Ting, D.S.K. A wind tunnel study on the aerodynamic interaction of vertical axis wind turbines in array configurations. *Renew. Energy* **2016**, *96*, 904–913. [CrossRef]
4. Vergaerde, A.; De Troyer, T.; Kluczewska-Bordier, J.; Parneix, N.; Silvert, F.; Runacres, M.C. Wind tunnel experiments of a pair of interacting vertical-axis wind turbines. *J. Phys. Conf. Ser.* **2018**, *1037*, 072049.[CrossRef]
5. Vergaerde, A.; De Troyer, T.; Standaert, L.; Kluczewska-Bordier, J.; Pitance, D.; Immas, A.; Silvert, F.; Runacres, M.C. Experimental validation of the power enhancement of a pair of vertical-axis wind turbines. *Renew. Energy* **2020**, *146*, 181–187. [CrossRef]
6. Jiang, Y.; Zhao, P.; Stoesser, T.; Wang, K.; Zou, L. Experimental and numerical investigation of twin vertical axis wind turbines with a deflector. *Energy Convers. Manag.* **2020**, *209*, 112588. [CrossRef]
7. Jodai, Y.; Hara, Y.; Sogo, Y.; Marusasa, K.; Okinaga, T. Wind tunnel experiments on interaction between two closely spaced vertical axis wind turbines. In Proceedings of the 23rd Chu-Shikoku-Kyushu Branch Meeting, The Japan Society of Fluid Mechanics, Yamaguchi, Japan, 1–2 June 2019; pp. 11-1–11-2.
8. Jodai, Y.; Hara, Y. Wind Tunnel Experiments on Interaction between Two Closely Spaced Vertical-Axis Wind Turbines in Side-by-Side Arrangement. *Energies* **2021**, *14*, 7874. [CrossRef]
9. Zanforlin, S.; Nishino, T. Fluid dynamic mechanisms of enhanced power generation by closely spaced vertical axis wind turbines. *Renew. Energy* **2016**, *99*, 1213–1226. [CrossRef]
10. Chen, W.H.; Chen, C.Y.; Huang, C.Y.; Hwang, C.J. Power output analysis and optimization of two straight-bladed vertical-axis wind turbines. *Appl. Energy* **2017**, *185*, 223–232. [CrossRef]
11. De Tavernier, D.; Ferreira, C.; Li, A.; Paulsen, U.S.; Madsen, H.A. Towards the understanding of vertical-axis wind turbines in double-rotor configuration. *J. Phys. Conf. Ser.* **2018**, *1037*, 022015. [CrossRef]
12. Ma, Y.; Hu, C.; Li, Y.; Li, L.; Deng, R.; Jiang, D. Hydrodynamic Performance Analysis of the Vertical Axis Twin-Rotor Tidal Current Turbine. *Water* **2018**, *10*, 1694. [CrossRef]
13. Hara, Y.; Jodai, Y.; Okinaga, T.; Sogo, Y.; Kitoro, T.; Marusasa, K. A synchronization phenomenon of two closely spaced vertical axis wind turbines. In Proceedings of the 25th Chu-Shikoku-Kyushu Branch Meeting, The Japan Society of Fluid Mechanics, Takamatsu, Japan, 31 May 2020; pp. 3-1–3-2.
14. Hara, Y.; Jodai, Y.; Okinaga, T.; Furukawa, M. Numerical Analysis of the Dynamic Interaction between Two Closely Spaced Vertical-Axis Wind Turbines. *Energies* **2021**, *14*, 2286. [CrossRef]
15. Jin, G.; Zong, Z.; Jiang, Y.; Zou, L. Aerodynamic analysis of side-by-side placed twin vertical-axis wind turbines. *Ocean Eng.* **2020**, *209*, 107296. [CrossRef]
16. Whittlesey, R.W.; Liska, S.; Dabiri, J.O. Fish schooling as a basis for vertical axis wind turbine farm design. *Bioinspir. Biomimetics* **2010**, *5*, 035005. [CrossRef] [PubMed]
17. Novak, P.; Ekelund, T.; Jovik, I.; Schmidtbauer, B. Modeling and control of variable-speed wind-turbine drive-system dynamics. *IEEE Control Syst. Mag.* **1995**, *15*, 28–38. [CrossRef]